

Cite this: *J. Mater. Chem. A*, 2018, 6, 4822

Single-crystal-like optoelectronic-properties of MAPbI₃ perovskite polycrystalline thin films†

Nadja Giesbrecht,^a Johannes Schlipf,^b Irene Grill,^a Philipp Rieder,^c Vladimir Dyakonov,^{cd} Thomas Bein,^a Achim Hartschuh,^a Peter Müller-Buschbaum^b and Pablo Docampo^{*ae}

Our understanding of the crystallization process of hybrid halide perovskites has propelled the efficiency of state-of-the-art photovoltaic devices to over 22%. Further improvements to the performance will likely arise from reducing the number of grain boundaries. Here, current methods lead to grain sizes in the 1 micrometer range and the resulting optoelectronic properties suffer as compared to single-crystal materials. In this work, we introduce a new synthesis procedure with MAPbI₃ leading to crystal sizes in the tens of microns range. This approach is based on the pre-crystallization of an intermediate phase (IP) based on the solid-state reaction of a lead-acetate trihydrate precursor mixture in a highly polar solvent. Beyond large grain sizes, the crystal orientation is also tightly controlled, leading to perovskite crystallites which remain perfectly aligned with the c-axis of the tetragonal structure parallel to the substrate as evidenced by grazing incidence wide angle X-ray scattering (GIWAXS). Furthermore, we demonstrate the high crystallinity and large grain size of the developed films via high-resolution transmission electron microscopy (HRTEM). The charge carrier mobilities are significantly improved with larger grain size and approach mobility values of about 40 cm² V⁻¹ s⁻¹, moving toward the values observed for single crystals. We capitalize on the enhanced optoelectronic properties of the developed films by incorporating them into planar heterojunction solar cells which reach power conversion efficiencies of 18.5%, higher than MAPbI₃-based device prepared from standard methods in a like-to-like comparison.

Received 22nd December 2017
Accepted 4th February 2018

DOI: 10.1039/c7ta11190h

rsc.li/materials-a

Introduction

Hybrid halide perovskite materials have galvanized the photovoltaic community due to their unprecedented easy and low-cost fabrication combined with remarkable optoelectronic properties, reminiscent of GaAs.^{1,2} Polycrystalline perovskite-based photovoltaic devices already reach efficiencies above 22% after extensive optimization of the perovskite film morphology and composition and engineering of the film interfaces.^{3–6} However, the density of grain boundaries in those polycrystalline perovskite films is still rather high, which places a constraint on the charge transport properties of the perovskite

films and ultimately will limit the maximum achievable device performance.⁷

Single crystals of perovskite materials show a dramatic improvement of all properties, including charge carrier mobility, charge carrier diffusion length, and a substantially reduced defect density.^{8–11} Therefore, a higher performance can be expected with single crystalline perovskite absorber layers, as is the case for Si- or GaAs-based photovoltaic devices.¹² However, the growth of single crystalline thin perovskite films is challenging^{13–15} and the forced lateral architecture with sequentially deposited electrodes, charge extraction material and buffer layers is usually required. Such devices to date do not show competitive efficiencies.^{13,16} Instead, the main improvement to perovskite solar cells has risen as a result of the development of novel synthesis methods focussing on polycrystalline films with vertical device stack architectures.^{3,17} Nevertheless, in order to facilitate further progress in the performance of perovskite solar cells, we must tap into the full potential of perovskite materials by targeting thin films that exhibit properties similar to those of single crystals, *i.e.* macroscopic crystal grains and minimum disorder at the grain boundaries.

To this end, a precise control of orientation and morphology of polycrystalline films will be necessary. Currently, a plethora of deposition methods is being developed and studied for the

^aDepartment of Chemistry and Center for NanoScience (CeNS), University of Munich (LMU), Butenandstr. 5-13, 81377 München, Germany

^bLehrstuhl für Funktionelle Materialien, Physik-Department, Technische Universität München, James-Frank-Str. 1, 85748 Garching, Germany

^cExperimental Physics VI, Julius Maximilian University of Würzburg, 97074 Würzburg, Germany

^dBavarian Center for Applied Energy Research (ZAE Bayern), 97074 Würzburg, Germany

^eSchool of Electrical and Electronic Engineering, Newcastle University, Merz court, NE1 7RU, Newcastle upon Tyne, UK. E-mail: Pablo.Docampo@newcastle.ac.uk

† Electronic supplementary information (ESI) available. See DOI: 10.1039/c7ta11190h

methylammonium lead iodide (MAPbI₃) compound. In particular, the crystallization kinetics and dynamics were investigated with different lead(II)-precursors and different methylammonium iodide (MAI) ratios^{18–21} or different solvents for the precursor solution, in both one and two-step approaches.^{22–27} In general, the crystallization kinetics can be divided into three categories: (i) direct formation of the perovskite material from a precursor solution mixture, (ii) sequential addition of the perovskite components or (iii) formation of an intermediate crystalline or amorphous phase which is then converted into the perovskite phase. Employing the first method leads to little control of the morphology, albeit rather large crystals can be formed if an ionic liquid or the anti-solvent technique is used.^{28,29} Employing a sequential deposition approach (ii) generally leads to small grain sizes in the range of hundreds of nanometres.³⁰ The formation of an intermediate phase (iii), especially the Pb-dimethylsulfoxide (DMSO) complex³ so far resulted in perovskite films showing highest efficiencies in perovskite solar cells. However, the intermediate phase is formed from solution and is highly unstable.³¹ Therefore, this approach usually lacks fine control of perovskite phase formation and does not lead to perovskite grain sizes exceeding 1 μm.^{3,22–24,32}

Larger grain sizes have been already reached for MAPbBr₃ based thin films in our previous work based on the use of the lead acetate precursor.³³ Grain sizes larger than 10 μm were achieved in a smooth thin film comprising perfectly aligned crystals with respect to the substrate. For MAPbI₃ films, so far only crystal sizes in the nanometer range were synthesized with the use of the lead acetate precursor. However, two independent studies showed that if using the PbAc₂ precursor, the amount of hydration water during perovskite synthesis is essential for optimized photovoltaic performance of the employed perovskite films in devices.^{34,35} Thus, the role of the hydration water for the perovskite synthesis needs to be understood to further improve this synthesis strategy.

In this paper, we introduce a new crystallization strategy based on lead acetate trihydrate. Dissolving this precursor mixture in a highly polar solvent, such as tetrahydrothiophene 1-oxide, leads to the formation of an air-stable intermediate phase that can be converted into the perovskite phase upon heating. We controlled the crystallization process by reducing the nucleation rate significantly and triggering fast perovskite crystal growth with the annealing step, leading to grain sizes of over 10 μm in a homogeneous thin film. Such increase in grain size and orientation leads to remarkably enhanced electrical properties of the polycrystalline perovskite films reaching single-crystalline properties, such as charge carrier mobility values in the range of 40 cm² V⁻¹ s⁻¹. When introduced into devices, polycrystalline films grown using the new approach resulted in power conversion efficiency values above 18.5%, significantly above those found for traditional approaches in a like-to-like comparison.

Results and discussion

The MAPbI₃ thin films developed in this work are based on a new synthetic protocol using lead acetate trihydrate in

combination with a highly polar solvent, tetrahydrothiophene-1-oxide (THTO). Briefly, the solid precursors are mixed in the solid form and then the solvent mixture dimethylformamide (DMF)/THTO is added. To form the MAPbI₃ films the solution was spin-coated at 5000 rpm for 180 s on top of the substrate and annealed at 130 °C for 5 min (see the ESI† for all details).

The crucial step in the film formation process is mixing the precursor in the solid state prior to adding the solvent mixture. As shown in Fig. 1a, the colourless precursor mixture becomes yellow after manually shaking the vial. This leads to the formation of a highly crystalline intermediate phase (IP) with the crystal structure shown in Fig. 1b. In the XRD pattern of the new phase, we see no presence of the precursor phases, indicating a phase-pure new compound that can be indexed to an orthorhombic structure with a space group similar to *P222* with lattice parameters *a* = 6.4 Å, *b* = 15.935 Å, and *c* = 27.805 Å. We note that the formation of the IP relies on the presence of hydration water in the lead acetate precursor. The XRD analysis in the ESI† of the precursor mixture using dehydrated PbAc₂ shows that no new phase is formed (*cf.* Fig. S1a†). This is not unexpected, as different groups found hydration water in the lead acetate precursor to be necessary to crystallize high-performing perovskite films in photovoltaic devices.^{34,35}

To further study this new IP and its structure we crystallized it from water. We found that the crystals growth is anisotropic with very long lengths in the mm range but widths in the nm range as shown in Fig. 1c and in the ESI (Fig. S1d†). Our 2D XRD data show similarity to an (MA⁺)₂(PbI₃⁻)₂PbI₂·2DMSO phase from a synthesis *via* a polymeric plumbate(II) fiber identified by Guo *et al.*³¹ We note that this approach can also be used for bromide instead iodide, as shown in the ESI.† In contrast to the Pb-DMSO complex, the IP shown here is very stable at ambient conditions and directly converts to the perovskite phase if heated to at least 80 °C.

To deposit the IP from the solution the choice of solvent is highly important. The most commonly used solvents such as DMF or γ -butyrolactone (GBL) do not favour the formation of the IP^{18,34,36} but instead result in fast perovskite crystallization, as can be seen in Fig. S2a.†²¹ Therefore, the solvent mixture needs to be modified to promote the crystallization of the IP rather than the perovskite phase. This is achieved by simply increasing the solubility of the perovskite compared to the solubility of the IP. Foley *et al.* predicted with Mayer bond order calculations a slightly more negative enthalpy of perovskite solvation for DMSO compared to DMF and a much more negative enthalpy of solvation for THTO.²⁷

To find a suitable solvent mixture, we studied the crystallization behaviour from a range of solvents *via in situ* XRD measurements at ambient conditions right after spin-coating the films in a nitrogen-filled glovebox. DMF-based solutions lead to a highly crystalline perovskite phase immediately after spin-coating. However a weak reflection at around 9.6°, *2* θ indicates the presence of a second phase which corresponds to the IP. Employing DMSO, as shown in Fig. S2b,† leads to slower perovskite crystallization and a higher amount of the intermediate phase. Here, increasing the DMSO concentration leads to a competition of the lead-DMSO complex (as shown in ESI†) and

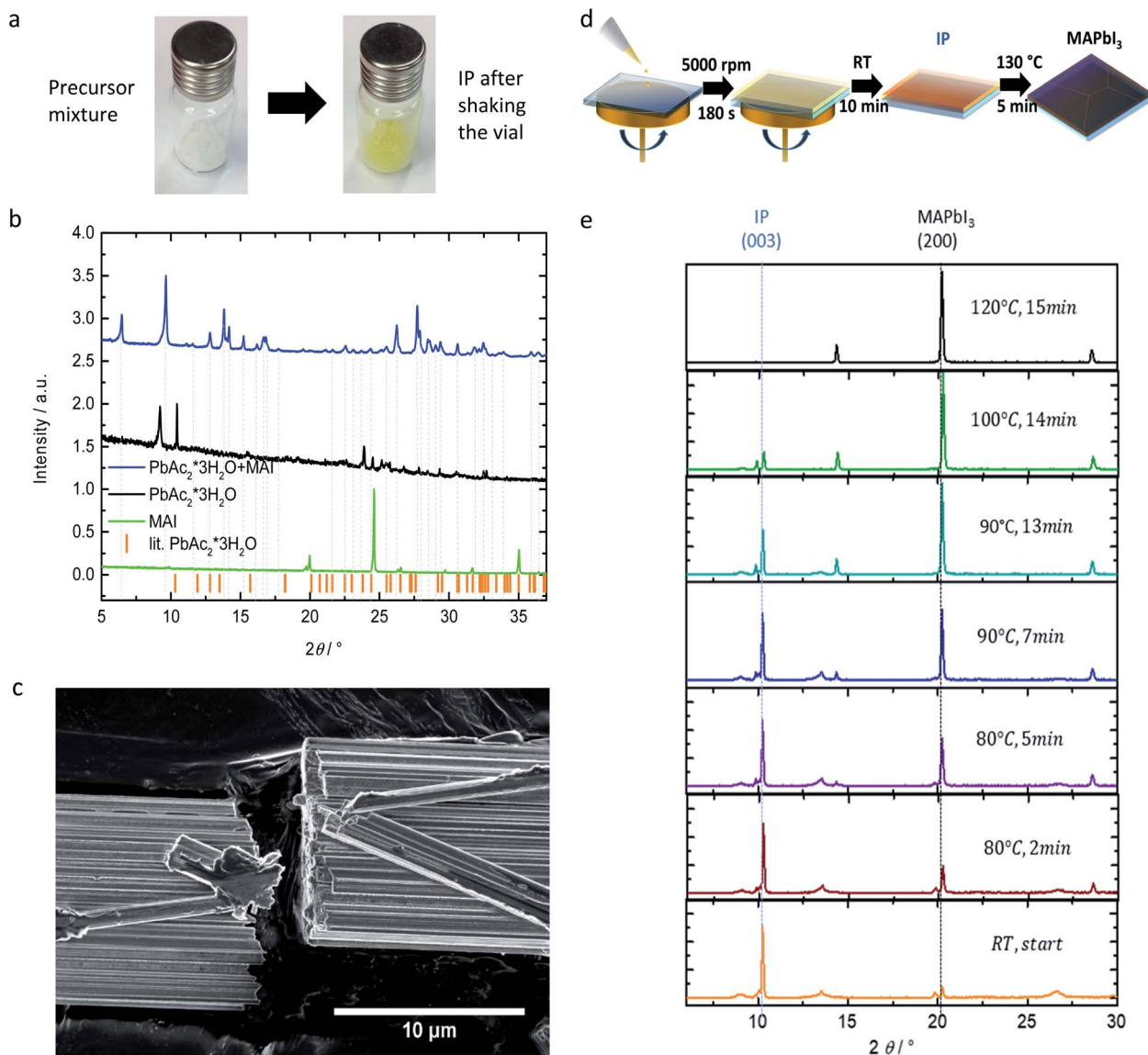


Fig. 1 (a) Photos of the precursor mixtures before and after shaking of the vial; (b) comparison of the precursors MAI and (hydrated) $\text{PbAc}_2 \cdot 3\text{H}_2\text{O}$ with resulting new intermediate phase (IP) compound from mixing both solids; (c) SEM image of the needle shaped crystals from the IP; (d) Schematic illustration of the spin-coating process; (e) *in situ* XRD while annealing the substrate with the spin-coated precursor solution.

therefore inhibited crystallization of the new IP. Finally, THTO does not form any additional intermediate phases from the perovskite precursor solution and small concentrations around 10–13 vol% are already sufficient to prevent perovskite nucleation before the IP is fully crystallized (see Fig. S2c–f†). In Fig. 2d a schematic illustration of the final synthesis process through the IP phase is illustrated.

The *in situ* XRD data collected in Fig. 1e clearly show the direct transformation of the (003) reflection of the IP to the (200) reflection of the perovskite. Initially, the IP shows the (003) reflection at 10° , which shifts to 9.6° upon complete drying as shown in the ESI.† At this stage, the IP is completely stable under ambient conditions with the same structure as from solid state reaction from the precursors. We note that the IP in the film is highly oriented and therefore mainly the reflection at

9.6° is visible. To confirm that the IP is the same in both cases, we have compared the XRD between powder from the precursor mixture and powder scraped off from the film, showing the same crystallographic pattern (see Fig. S1b†).

To inhibit the perovskite nucleation and promote the crystallization of the IP from solution, the addition of THTO to the solvent mixture is crucial. This, in turn, influences the resulting grain size by determining the number of potential nucleation points for perovskite phase conversion as shown in Fig. 2. Grain sizes of up to $100 \mu\text{m}$ can be reached with 26 vol% THTO additive but the films show poor grain interconnection and smoothness. We found the best compromise between grain size and overall film quality to be reached with perovskite films obtained from 13 vol% THTO. This mixture leads to grain sizes of above $10 \mu\text{m}$ in a very dense and smooth film when annealed

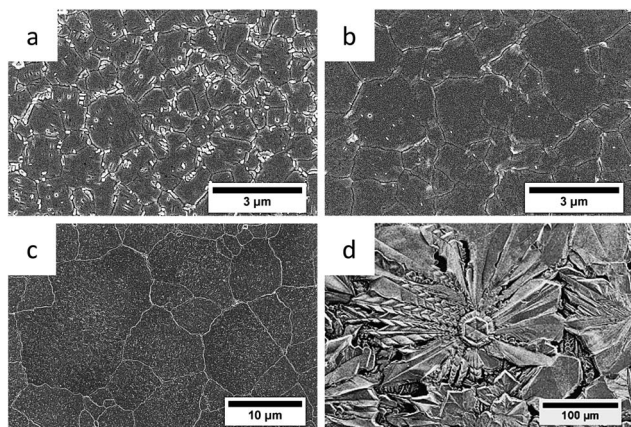


Fig. 2 SEM images of perovskite films prepared from different THTO concentrations: (a) 7 vol% THTO; (b) 10 vol% THTO; (c) 13 vol% THTO; (d) 26 vol% THTO.

at 130 °C. Somewhat surprisingly, lower annealing temperatures and longer conversion times lead to smaller crystallites as shown in the ESI†

To obtain more insights regarding crystal orientation we performed grazing-incidence wide-angle X-ray scattering (GIWAXS) measurements, see Fig. 3a. GIWAXS is a powerful method for evaluation of crystal orientation in thin films due to the high statistical relevance and the possibility to extract quantitative information about the crystalline part of the sample.^{37–39} A typical sample based on lead acetate and employing DMF solvent usually shows no preferential orientation as shown in literature and in the ESI† for films prepared under our synthesis conditions.^{35,36,40} As shown earlier by Foley *et al.*, the solvent THTO, on the other hand, can be used to achieve a high degree of orientation in MAPbI₃ films.²⁷ They argue that homogeneous nucleation is suppressed and instead heterogeneous nucleation starting at the substrate is responsible for this orientation. Here the synthesis parameters are different since the perovskite is formed through an IP.

However, with increased THTO concentration, the perovskite crystal alignment within the film is confined to the (200) facet parallel to the substrate as explained in the following: Fig. 3a shows the 2D GIWAXS pattern of a film with 13 vol% THTO. The strong preferential orientation of the MAPbI₃ crystallites is apparent from the individual scattering reflections which are labeled according to the crystal planes from which they originate. The splitting of the cubic (110) and (111) peaks gives rise to the (112)/(200) and the (211)/(202) pair of peaks, respectively, and shows that the sample is in tetragonal phase. In comparison, in the 2D GIWAXS pattern of the sample prepared from pure DMF solvent the reflections adopt the form of Debye-Scherrer rings indicating no preferential crystal orientation (*cf.* Fig. S4c†).

Azimuthal line cuts around the q range of the (002)/(110) and their second order peaks (004)/(220) of the 13 vol% THTO data are plotted with intensity *vs.* azimuthal angle χ in Fig. S4b.† From the intensity distribution in these cuts, the orientation of crystals in the film can be evaluated statistically. Therefore, the

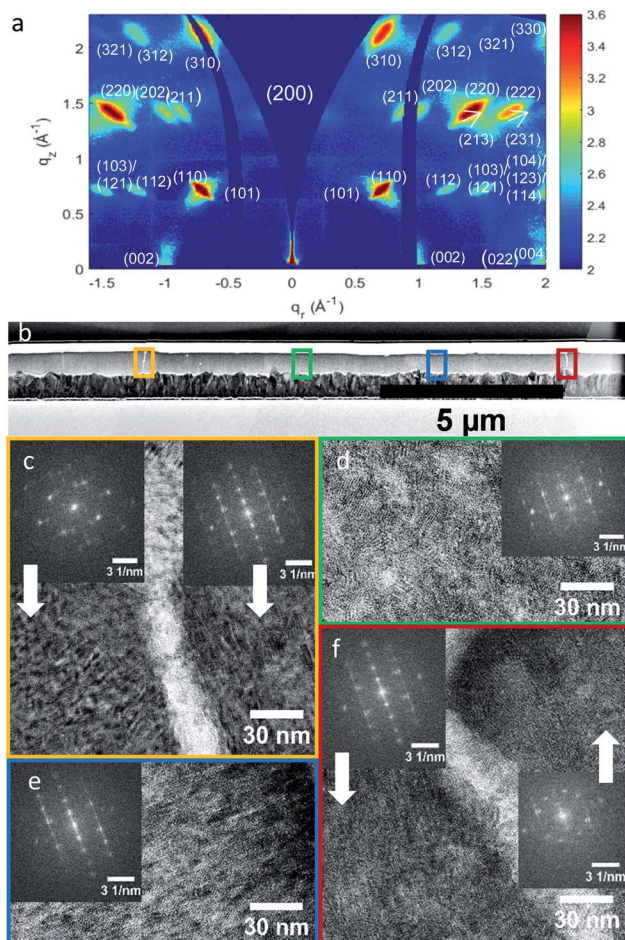


Fig. 3 (a) 2D GIWAXS pattern of a sample prepared from 13 vol% THTO solvent additive to the precursor solution shown in q_r – q_z representation; (b) TEM cross-section of the lamella incorporating a MAPbI₃ film deposited from 13 vol% THTO; (c–f) HRTEM's and their FFT's from the spots marked in (b).

peaks were fitted with Voigt functions and their positions was determined to be 44.8(3)°. These peak positions verify that the sample is oriented with the (200) facet parallel to the substrate which can be imagined as a cuboid lying on its side. The extremely narrow FWHM of 2.0(7)° of these Voigt functions shows how well the MAPbI₃ crystals are aligned inside the film. As seen in Fig. S5,† already 10 vol% of THTO additive is sufficient for strong crystal alignment and 13 vol% THTO is optimal for pure crystal alignment verifying the GIWAXS result.

To determine the actual grain size within the perovskite film we performed high resolution transmission electron microscopy (HRTEM) on a cross-section of a photovoltaic device. To this end, we cut a 45 μm long lamella with a focused ion beam from a complete solar cell device in FTO/TiO₂/MAPbI₃/Spiro-OMeTAD/Au architecture (see the ESI† for the full analysis). In Fig. 3 we show a representative area of a 16 μm long TEM cross-section. Here, HRTEM images from four different spots are shown together with their fast Fourier transform (FFT). A change in pattern can only be observed at bright regions between the grains. Thus, we assume the bright lines to be the

grain boundaries. In the image, the FFT pattern along the 12 μm distance between the bright areas does not change, indicating that it is indeed a single crystal. Our results show that there are mainly two distinct crystal orientations in the in-plane direction in this sample, confirming the high degree of order in the material. We note that the samples are highly sensitive to the electron beam and particularly the grain boundaries become broader with longer illumination times.

To additionally classify the different layers in the cross-section, we performed energy-dispersive X-ray spectroscopy (EDX) during the TEM investigation, as shown in Fig. S7.† Here, we can clearly distinguish between our different layers in the stack with the distribution of different atoms present and detectable. We see no heterogeneity in our perovskite layers, confirming their high quality.

To quantify the improvement in optoelectronic properties with larger grains in our polycrystalline films we performed Time of Flight (ToF) measurements as shown in Fig. 4. ToF measurements were performed in a lateral sample configuration where the different MAPbI₃ films were deposited on top of an in-plane gold contact pattern. Here, the photogenerated carriers can be extracted from the electrodes with varying spacing d in the range of several tens of micrometers. Charge carrier generation is induced upon pulsed laser excitation at the margin of one contact while drift of the charges occurs due to an external DC field ($E = 5 \text{ kV cm}^{-1}$) which is applied only during the short measurement period of the $j-t$ profile. Since the charges are created locally near one electrode, the polarity of the E-field defines whether electron or hole transport across the material is observed. A detailed description of the employed setup can be found in the ESI.†

Representative transients obtained for different electrode spacings are shown in Fig. 4a. Following a fitting procedure for ToF transients,⁴¹ the transit time t_{tr} was extracted and plotted as a function of d for every investigated material (Fig. 4b). Because of the linear dependence of t_{tr} on d , the mobility can be calculated from the respective fit according to $\mu = d/(E \times t_{\text{tr}})$. The determined values are listed in Table 1. Clearly, an influence of the grain size is observable.

With increasing grain size the mobility values increase, indicating improved transport properties due to a reduced number of grain boundaries which represent potential recombination sites.⁷ We note that a full analysis of the 26 vol% THTO sample was not possible due to a large number of pinholes in the film. Therefore, the photocurrent in this device was only measurable for a small amount of different electrode spacings with no representative trend from the obtained transients. The value presented here was obtained from a voltage series performed on a fixed gap size where the photocurrent was detectable (see Fig. S8†) and represents a lower limit of the mobility. We further note that the

Table 1 Extracted mobility values from ToF measurement showing increasing charge mobility with grain size. The 26 vol% sample (*) was measured with a different procedure as discussed in the ESI

THTO conc./vol%	Hole mobility/ $\text{cm}^2 (\text{V s})^{-1}$	Electron mobility/ $\text{cm}^2 (\text{V s})^{-1}$	Stand. Dev.	Sum/ $\text{cm}^2 (\text{V s})^{-1}$
0	8	9	1	17
7	11	12	1	23
10	13	13	1	26
13	15	17	1	32
26*	17*	23*		40*

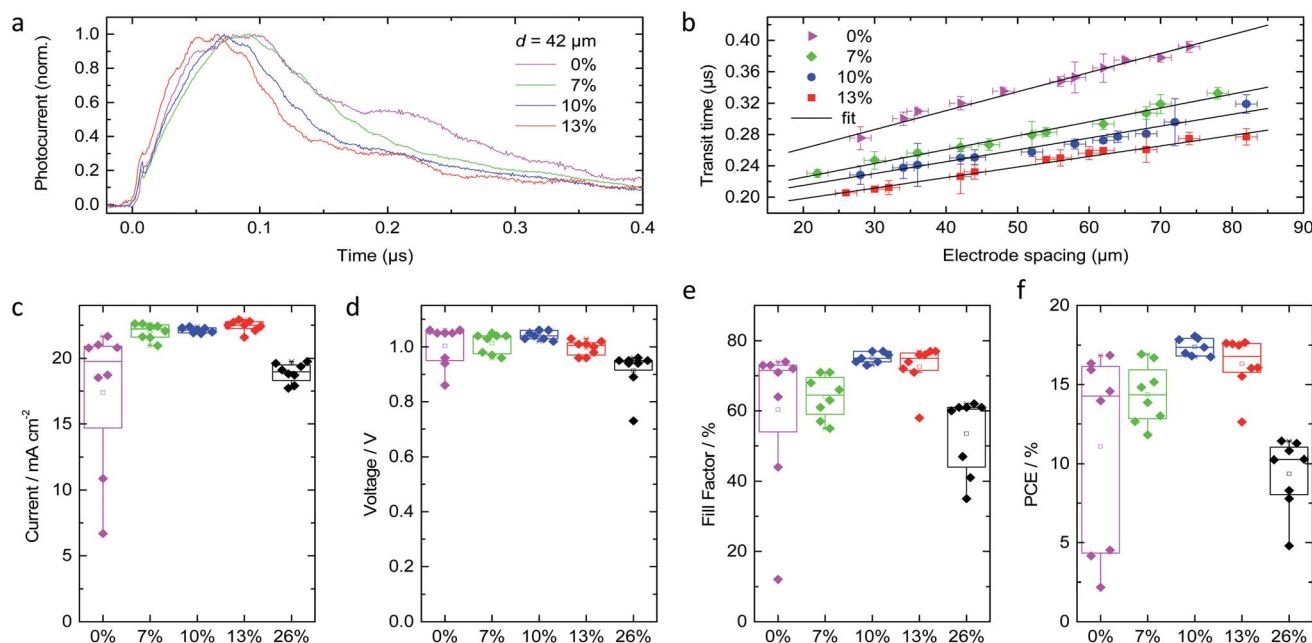


Fig. 4 (a) Representative transients obtained at 42 μm spacing; (b) extracted transit times for holes from ToF with perovskite films deposited from different THTO concentrations; (c–f) device performance deviation of devices in the architecture FTO/TiO₂/C₆₀/Al₂O₃/MAPbI₃/Spiro-OMeTAD/Au employing perovskite films deposited from different THTO concentrations.

transport measurement in the lateral configuration is essential to gain information on the optoelectronic properties of the perovskite layer, while vertical in-plane devices show several limitations for data acquisition.⁴² Additionally, our sample configuration allows for the measurement of charge transport on a macroscopic scale over several micrometres reflecting the influence of grain boundaries and defects, which directly affects charge carrier transport.

In order to study the effect of crystal size on solar cell performance, we prepared devices in a planar heterojunction configuration (FTO/TiO₂/C₆₀/Al₂O₃/MAPbI₃/Spiro-OMeTAD/Au). We show a box plot distribution of the device performance of at least 8 devices for the different perovskite films in Fig. 4. Here, we mainly observe an increase in fill factor (FF), correlating with the improved electrical properties of the bigger crystal films. We note that for devices fabricated from films with crystal sizes above 3 μm (namely 10 vol% and 13 vol% THTO), no significant difference in device performance occurs. The performance of these two samples is in fact within the experimental error of the system and show the highest value at 18.5% as well as the highest reproducibility. The high short-circuit current densities above 22 mA cm⁻², which are gained in these devices correlate perfectly with the current calculated from EQE measurement of 22.45 mA cm⁻² (see Fig. S9†). We however note that all the devices employing architectures as shown in Fig. 4 have high hysteresis with non-stabilized power output. This instability is probably related to the charge extraction layers and not the perovskite layer, since with devices employing different transport materials such as poly(3,4-ethylenedioxythiophene)-poly(styrenesulfonate) (PEDOT:PSS) or [6,6]-phenyl C₆₁ butyric acid methyl ester (PCBM) demonstrated minimal hysteresis and stabilized power output, as can be seen in Fig. S9.†

The perovskite films with the largest grain sizes contain a large number of pinholes which leads to semi-transparent films with an average transmittance of about 28% in the visible range, as shown in the ESI.† Therefore the device properties drop if these films are incorporated. However, the current density in these devices is extremely high with 19 mA cm⁻² on average which is much higher than for any reported semi-transparent MAPbI₃-based solar cells with a transmittance of about 20–30%.^{43–46} Hence, the device efficiency reaches very high values with the maximum at 12%, which is 4% higher than that of devices shown in the literature with semitransparent appearance due to pinholes.⁴³

Conclusions

In this work, we introduce a new route to deposit hybrid perovskite films with extremely large and perfectly oriented crystalline domains of 10–40 μm in size. In order to achieve this, we targeted a new, highly stable intermediate phase based on lead acetate trihydrate. Importantly, we find that a highly polar solvent, such as tetrahydrothiophene 1-oxide is necessary to inhibit the perovskite phase growth and to favour the crystallization of the IP. With HRTEM we can clearly identify the grain boundaries and verify high crystallinity and order within the

perovskite film. The newly developed films show charge transport properties similar to those found in perovskite single crystals with very high mobility values in the 40 cm² V⁻¹ s⁻¹ range. We capitalized on these improved properties by fabricating solar cells with a planar heterojunction architecture. The highly oriented and large grains lead to a power conversion efficiency of 18.5%, higher than what is achieved with standard fabrication in a like-to-like comparison.

Conflicts of interest

There are no conflicts to declare.

Acknowledgements

The authors acknowledge funding from the German Federal Ministry of Education and Research (BMBF) under the agreement number 03SF0516B and 03SF0514A, the Bavarian Ministry of the Environment and Consumer Protection, the Bavarian Network “Solar Technologies Go Hybrid” (SolTech) and the DFG Excellence Cluster Nanosystems Initiative Munich (NIM). The authors thank Dr Steffen Schmidt for the preparation of the FIB lamella, Dr Markus Döblinger for the transmission electron microscopy and Dr Andreas Baumann for technical assistance.

Notes and references

- H. J. Snaith, *J. Phys. Chem. Lett.*, 2013, **4**, 3623–3630.
- G. J. Bauhuis, P. Mulder, E. J. Haverkamp, J. C. C. M. Huijben and J. J. Schermer, *Sol. Energy Mater. Sol. Cells*, 2009, **93**, 1488–1491.
- W. S. Yang, B.-W. Park, E. H. Jung, N. J. Jeon, Y. C. Kim, D. U. Lee, S. S. Shin, J. Seo, E. K. Kim, J. H. Noh and S. I. Seok, *Science*, 2017, **356**, 1376–1379.
- H. Tan, A. Jain, O. Voznyy, X. Lan, F. P. García de Arquer, J. Z. Fan, R. Quintero-Bermudez, M. Yuan, B. Zhang, Y. Zhao, F. Fan, P. Li, L. N. Quan, Y. Zhao, Z.-H. Lu, Z. Yang, S. Hoogland and E. H. Sargent, *Science*, 2017, **355**, 722–726.
- J.-P. Correa-Baena, W. Tress, K. Domanski, E. H. Anaraki, S.-H. Turren-Cruz, B. Roose, P. P. Boix, M. Gratzel, M. Saliba, A. Abate and A. Hagfeldt, *Energy Environ. Sci.*, 2017, **10**, 1207–1212.
- M. He, B. Li, X. Cui, B. Jiang, Y. He, Y. Chen, D. O’Neil, P. Szymanski, M. A. El-Sayed, J. Huang and Z. Lin, *Nat. Commun.*, 2017, **8**, 16045.
- N. Cho, F. Li, B. Turedi, L. Sinatra, S. P. Sarmah, M. R. Parida, M. I. Saidaminov, B. Murali, V. M. Burlakov, A. Goriely, O. F. Mohammed, T. Wu and O. M. Bakr, *Nat. Commun.*, 2016, **7**, 13407.
- Q. Dong, Y. Fang, Y. Shao, P. Mulligan, J. Qiu, L. Cao and J. Huang, *Science*, 2015, **347**, 967–970.
- D. Shi, V. Adinolfi, R. Comin, M. Yuan, E. Alarousu, A. Buin, Y. Chen, S. Hoogland, A. Rothenberger, K. Katsiev, Y. Losovyj, X. Zhang, P. A. Dowben, O. F. Mohammed, E. H. Sargent and O. M. Bakr, *Science*, 2015, **347**, 519–522.

- 10 M. I. Saidaminov, V. Adinolfi, R. Comin, A. L. Abdelhady, W. Peng, I. Dursun, M. Yuan, S. Hoogland, E. H. Sargent and O. M. Bakr, *Nat. Commun.*, 2015, **6**, 7586.
- 11 A. A. Zhumekenov, M. I. Saidaminov, M. A. Haque, E. Alarousu, S. P. Sarmah, B. Murali, I. Dursun, X.-H. Miao, A. L. Abdelhady, T. Wu, O. F. Mohammed and O. M. Bakr, *ACS Energy Lett.*, 2016, **1**, 32–37.
- 12 National Renewable Energy Laboratory, *Research Cell Record Efficiency Chart*, 2017, <https://www.nrel.gov/pv/assets/images/efficiency-chart.png>.
- 13 L. Lee, J. Baek, K. S. Park, Y.-E. Lee, N. K. Shrestha and M. M. Sung, *Nat. Commun.*, 2017, **8**, 15882.
- 14 W. Wei, Y. Zhang, Q. Xu, H. Wei, Y. Fang, Q. Wang, Y. Deng, T. Li, A. Gruverman, L. Cao and J. Huang, *Nat. Photonics*, 2017, **11**, 315.
- 15 J. Chen, D. J. Morrow, Y. Fu, W. Zheng, Y. Zhao, L. Dang, M. J. Stolt, D. D. Kohler, X. Wang, K. J. Czech, M. P. Hautzinger, S. Shen, L. Guo, A. Pan, J. C. Wright and S. Jin, *J. Am. Chem. Soc.*, 2017, **139**, 13525–13532.
- 16 A. N. Jumabekov, E. Della Gaspera, Z. Q. Xu, A. S. R. Chesman, J. van Embden, S. A. Bonke, Q. Bao, D. Vak and U. Bach, *J. Mater. Chem. C*, 2016, **4**, 3125–3130.
- 17 Y. Wu, F. Xie, H. Chen, X. Yang, H. Su, M. Cai, Z. Zhou, T. Noda and L. Han, *Adv. Mater.*, 2017, **29**, 1701073.
- 18 W. Zhang, M. Saliba, D. T. Moore, S. K. Pathak, M. T. Hörantner, T. Stergiopoulos, S. D. Stranks, G. E. Eperon, J. A. Alexander-Webber, A. Abate, A. Sadhanala, S. Yao, Y. Chen, R. H. Friend, L. A. Estroff, U. Wiesner and H. J. Snaith, *Nat. Commun.*, 2015, **6**, 6142.
- 19 F. K. Aldibaja, L. Badia, E. Mas-Marza, R. S. Sanchez, E. M. Barea and I. Mora-Sero, *J. Mater. Chem. A*, 2015, **3**, 9194.
- 20 R. Munir, A. D. Sheikh, M. Abdelsamie, H. Hu, L. Yu, K. Zhao, T. Kim, O. E. Tall, R. Li, D.-M. Smilgies and A. Amassian, *Adv. Mater.*, 2017, **29**, 1604113.
- 21 D. T. Moore, H. Sai, K. W. Tan, D.-M. Smilgies, W. Zhang, H. J. Snaith, U. Wiesner and L. A. Estroff, *J. Am. Chem. Soc.*, 2015, **137**, 2350–2358.
- 22 W. S. Yang, J. H. Noh, N. J. Jeon, Y. C. Kim, S. Ryu, J. Seo and S. I. Seok, *Science*, 2015, **348**, 1234–1237.
- 23 N. J. Jeon, J. H. Noh, Y. C. Kim, W. S. Yang, S. Ryu and S. I. Seok, *Nat. Mater.*, 2014, **13**, 897–903.
- 24 J. Cao, X. Jing, J. Yan, C. Hu, R. Chen, J. Yin, J. Li and N. Zheng, *J. Am. Chem. Soc.*, 2016, **138**, 9919.
- 25 N. Ahn, D.-Y. Son, I.-H. Jang, S. M. Kang, M. Choi and N.-G. Park, *J. Am. Chem. Soc.*, 2015, **137**, 8696–8699.
- 26 C. Fei, B. Li, R. Zhang, H. Fu, J. Tian and G. Cao, *Adv. Energy Mater.*, 2016, 1602017, DOI: 10.1002/aenm.201602017.
- 27 B. J. Foley, J. Girard, B. A. Sorenson, A. Z. Chen, J. Scott Niezgodna, M. R. Alpert, A. F. Harper, D.-M. Smilgies, P. Clancy, W. A. Saidi and J. J. Choi, *J. Mater. Chem. A*, 2017, **5**, 113–123.
- 28 D. T. Moore, K. W. Tan, H. Sai, K. P. Barteau, U. Wiesner and L. A. Estroff, *Chem. Mater.*, 2015, **27**, 3197–3199.
- 29 M. Xiao, F. Huang, W. Huang, Y. Dkhissi, Y. Zhu, J. Etheridge, A. Gray-Weale, U. Bach, Y.-B. Cheng and L. Spiccia, *Angew. Chem.*, 2014, **126**, 10056–10061.
- 30 P. Docampo, F. C. Hanusch, S. D. Stranks, M. Döblinger, J. M. Feckl, M. Ehrensperger, N. K. Minar, M. B. Johnston, H. J. Snaith and T. Bein, *Adv. Energy Mater.*, 2014, **4**, 1400355.
- 31 Y. Guo, K. Shoyama, W. Sato, Y. Matsuo, K. Inoue, K. Harano, C. Liu, H. Tanaka and E. Nakamura, *J. Am. Chem. Soc.*, 2015, **137**, 15907–15914.
- 32 X. Li, D. Bi, C. Yi, J.-D. Décoppet, J. Luo, S. M. Zakeeruddin, A. Hagfeldt and M. Grätzel, *Science*, 2016, **353**, 58–62.
- 33 N. Giesbrecht, J. Schlipf, L. Oesinghaus, A. Binek, T. Bein, P. Müller-Buschbaum and P. Docampo, *ACS Energy Lett.*, 2016, **1**, 150–154.
- 34 S. Bai, N. Sakai, W. Zhang, Z. Wang, J. T. W. Wang, F. Gao and H. J. Snaith, *Chem. Mater.*, 2017, **29**, 462–473.
- 35 L. Ling, S. Yuan, P. Wang, H. Zhang, L. Tu, J. Wang, Y. Zhan and L. Zheng, *Adv. Funct. Mater.*, 2016, **26**, 5028–5034.
- 36 D. Forgacs, M. Sessolo and H. J. Bolink, *J. Mater. Chem. A*, 2015, **3**, 14121–14125.
- 37 L. Oesinghaus, J. Schlipf, N. Giesbrecht, L. Song, Y. Hu, T. Bein, P. Docampo and P. Müller-Buschbaum, *Adv. Mater. Interfaces*, 2016, **3**, 1600403.
- 38 A. Hexemer and P. Müller-Buschbaum, *IUCrJ*, 2015, **2**, 106–125.
- 39 J. Schlipf and P. Müller-Buschbaum, *Adv. Energy Mater.*, 2017, **7**, 1700131.
- 40 L. Zhao, D. Luo, J. Wu, Q. Hu, W. Zhang, K. Chen, T. Liu, Y. Liu, Y. Zhang, F. Liu, T. P. Russell, H. J. Snaith, R. Zhu and Q. Gong, *Adv. Funct. Mater.*, 2016, **26**, 3508–3514.
- 41 H. Scher and E. W. Montroll, *Phys. Rev. B*, 1975, **12**, 2455–2477.
- 42 I. Grill, M. F. Aygüler, T. Bein, P. Docampo, N. F. Hartmann, M. Handloser and A. Hartschuh, *ACS Appl. Mater. Interfaces*, 2017, **9**, 37655–37661.
- 43 G. E. Eperon, V. M. Burlakov, A. Goriely and H. J. Snaith, *ACS Nano*, 2014, **8**, 591–598.
- 44 J. W. Jung, C.-C. Chueh and A. K. Y. Jen, *Adv. Energy Mater.*, 2015, **5**, 1500486.
- 45 F. Fu, T. Feurer, T. Jäger, E. Avancini, B. Bissig, S. Yoon, S. Buecheler and A. N. Tiwari, *Nat. Commun.*, 2015, **6**, 8932.
- 46 C. Roldan-Carmona, O. Malinkiewicz, R. Betancur, G. Longo, C. Momblona, F. Jaramillo, L. Camacho and H. J. Bolink, *Energy Environ. Sci.*, 2014, **7**, 2968–2973.